A SIMULATION APPROACH FOR SERIES PRODUCTION OF PLASMA-BASED ADDITIVE MANUFACTURING OF TI-6AL-4V COMPONENTS

M. BIELIK*, E. NEUBAUER*, M. KITZMANTEL*,
I. NEUBAUER**, E. KOZESCHNIK***

**RHP-Technology GmbH, 2444 Seibersdorf, Austria*
***Simufact engineering Gmbh, 21079 Hamburg, Germany*
****TU Wien, 1060 Vienna, Austria*

DOI 10.3217/978-3-85125-968-1-20

ABSTRACT

Plasma Metal Deposition (PMD®) is a variant of a directed energy deposition (DED) process that uses an arc welding process to additively manufacture metal components. This process is characterised by relatively high deposition rates, low restrictions regarding the build space, low investment, and operating costs, and is, therefore, predestined for the series production of large structural parts. Additionally, advances in machine development, path planning, and the use of structural welding simulations are bringing these additive manufacturing (AM) technologies into the focus of modern production strategies. To ensure the quality of additively manufactured components in an exactly reproducible manner is, however, a challenge. This requires the complete reproducibility of the manufacturing process and the materials used. This paper investigates the Plasma Metal Deposition manufacturing process of a small batch of Ti-6Al-4V components. Numerical approaches for predicting temperature fields, distortions and residual stresses are examined using the Finite Element (FE) software Simufact Welding 8.0. The focus of the investigations is on the numerical analysis of the influence of the manufacturing process on the mechanical behaviour for multi-layer components. As an outstanding example, the manufacturing of an aerospace bracket is presented.

Keywords: Additive Manufacturing, Direct Energy Deposition, Plasma Metal Deposition, Space, Aerospace, Ti-6Al-4V, Simufact Welding

INTRODUCTION

Additive manufacturing (AM) is a group of manufacturing technologies that build physical three-dimensional objects by successive addition of material. AM has shown substantial growth in recent years and it is assumed that the technology and the industry are reaching increasing market maturity. Therefore, a growing number of companies are using AM for customised products and series production [1]. Wire Arc Additive Manufacturing (WAAM) is an emerging technology that has become a very promising

alternative to high-value large metal components in various industries. The technology combines arc welding with wire feeding and is able to benefit from design freedom, buy-to-fly ratios as low as 1.8, potentially no constraints in size, and low cycle times [2], [3]. WAAM is a manufacturing technology similar to multi-pass welding, which can be used to build components such as flanges, brackets, rocket components, or printing directly on fabricated components, such as, a WAAM-printed fuselage with stiffening structures. Components are built layer-by-layer depositing the melted material along predefined welding paths creating the 3D printed structure. One of the limitations of the WAAM process, however, is the formation of distortions caused by the build-up of residual stress as a result of the large thermal gradients induced during the repeated melting and solidification of the material. Deformation and residual stresses of WAAM components (unclamped condition after the deposition process) have been studied extensively in [4]–[7] for titanium and steel structures. Residual stress is affecting several failure mechanisms including fracture and fatigue properties, stress corrosion cracking and distortion [8]. Thus, in order to optimise the WAAM process prior to the deposition and reduce residual stresses and distortion, a thermo-mechanical finite element (FE) model is set-up. By means of the simulation model, the temperature field, distortions, and residual stresses are predicted and analysed. The temperature field and its gradients have been determined by using Goldak's double ellipsoid heat source model [9]. For the verification of the FE models, measurements have been performed on the deposited components with regard to temperature field distributions and weld deformations. The acquired simulation results are used for the production of a near-net-shape aerospace bracket.

METHODOLOGY

MATERIALS AND SET-UP

Deposition experiments are performed on Ti-6Al-4V baseplates with dimensions of 200x50x10 mm. Cold Ti-6Al-4V wire with a diameter of 1.2 mm is fed by an automatic wire feeder. High purity argon (99.99 %) is used as shielding and plasma gas. Thin-walled samples (so called demonstrators) are manufactured by depositing a single row of successive weld beads along the centreline of plates. Both, baseplates and welding wire with chemical composition listed in Table 1 are commercially sourced conforming to ASTM B265 and AWS A5.16-07, respectively.

Table 1 Chemical composition of Ti-6Al-4V wire and base plates (wt.%)

	Ti	Al	V	Fe	C	N	H	O
Wire	Bal.	6.24	4.16	0.15	0.015	0.008	0.003	0.13
Base plates	Bal.	6.12	4.07	0.178	0.019	0.011	0.002	0.012

The equipment used for the welding process is shown in Fig. 1 (a) and consists of a complete WAAM system at RHP-Technology utilising plasma metal deposition. The AM process is enclosed in an airtight welding chamber filled with high purity argon with a

low moisture content, thus utilising a protective gas atmosphere and giving adequate shielding. In the case of oxygen sensitive materials, such as titanium, the encapsulated system allows manufacturing in a controlled environment, and potentially can reduce oxygen levels to less than 100 ppm. Two blind holes of 6 mm diameter are machined along the centreline of the base plates. These holes are used to additionally position the plates inside the working space and reference to the tool coordinate system (Fig. 1 (b)).

(a)

(b)

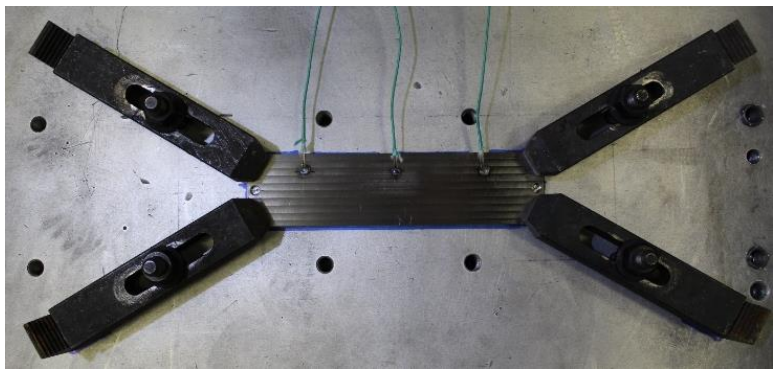

Fig. 1 (a) Model of the welding chamber; (b) Experimental set-up inside the PMD system

The baseplates are fixed to the backing plate of the WAAM system using four clamps placed at specified positions to ensure identical clamping conditions for all demonstrators. The studs are tightened crosswise with a torque of 80 Nm. Prior to the AM process, the baseplates are degreased and cleaned with acetone to eliminate surface contamination. Deposition is initiated below a residual oxygen content of less than 100 ppm O_2 measured

with a residual oxygen analyser OXY 3 by ORBITEC, which has a measuring range from 5ppm to 21 % O_2. A single track wide bidirectional deposition strategy is adopted, i.e., the starting point of the next layer is where the previous layer finished. Cold wire is fed by an automatic wire feeder transversal to the welding direction to avoid rotation of the torch. Although in-house research at RHP-Technology has shown that a feed mode, in which the wire is fed ahead of the arc yields more consistent weld beads, the transversal position is a good compromise for the bidirectional welding strategy. Further automation of the custom-made machine would be required to rotate the torch according to the direction of deposition. The deposition strategy is shown in Fig. 2, where the orange lines represent the movement of the torch. A standard reference coordinate system of the single wall is defined, in which x is parallel to the travel direction of the torch, y is the transverse direction, and z is parallel to the building direction of the wall. When the torch comes to the end of the weld bead, the arc is extinguished, the torch increases its height in z direction and remains in this park position for a defined cooling time. After the dwell time has elapsed, the torch moves in negative z direction towards the end position of the previous layer and starts to deposit a new layer in the reverse direction. Thereby, the distance between the torch and the deposited layers is kept constant at 10 mm. This process is repeated until a desired number of layers is deposited.

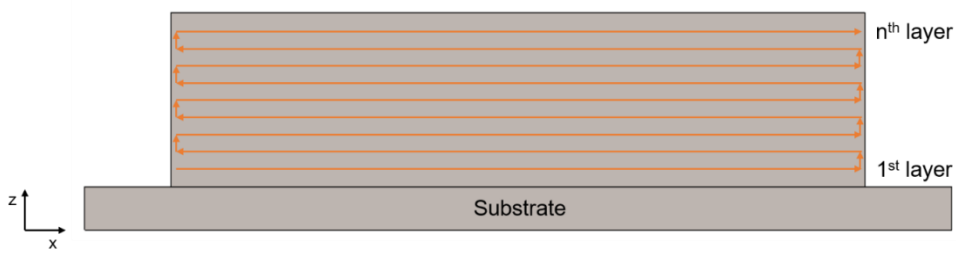

Fig. 2 Bidirectional building strategy

The bidirectional strategy aims to mitigate the inconsistency in wall height as reported by Martina et al. [2]. Using a unidirectional welding strategy, i.e., starting each layer at the same point, will cause a hump in the beginning and a depression towards the end of a wall. The same authors [2] attribute the depression at the end to a build-up of heat caused by the lack of heat sink in front of the torch and the hump in the beginning may be caused by thermal effects associated with the deposition on the cold base material.

Ten thin-walled demonstrators are manufactured to investigate post-process distortion and weld induced residual stresses, which are generated by the high thermal input of the PMD process. Demonstrators D1 and D2 are fabricated to test and adjust the welding parameters and are excluded from further analysis. Before deposition, all baseplates are preheated with two single passes of the arc without feeding wire to avoid the first single track to become too narrow and prevent separation of the wall from the baseplate. All demonstrators from D3 to D10 are deposited employing the same set of parameters, which are listed in Table 2.

Table 2 Deposition parameters

Description	Symbol	Preheating	Deposition	Unit
Wire diameter	d	-	1.2	[mm]
Welding current	I	130	140	[A]
Voltage	U	25	25	[V]
Travel speed	v_{TS}	300	200	[mm/min]
Feed rate	f	-	0.9	[kg/h]
Wire feed speed	v_{WFS}	-	2910	[mm/min]
Cooling time	t_{cool}	1	30	[s]
Total dwell time	t_{dwell}	9	38	[s]
Number of layers	N	2	32	[-]
Pilot gas		1.5	1.5	[l/min]
Shielding gas		5	5	[l/min]

IN SITU TEMPERATURE MEASUREMENT

In situ measurements of the temperature are made at three selected locations on top of the baseplates using 0.81 mm diameter type-K thermocouples provided by OMEGA, as shown in Fig. 3 (a). The thermocouples have a glass fibre isolation and an accuracy of ± 2.2 °C or ± 0.75 % in a temperature range from 0 to 1250 °C. The thermocouples are welded on the top surface of the baseplates to ensure a proper thermal contact and are covered with steel sleeves to shield them from the plasma (Fig. 3 (b)). Test runs have shown that a current can be induced through electro-magnetic effects of the plasma leading to noise in the data. In addition, the steel sleeves prevent the thermocouples from being exposed to the direct heat of the plasma which can lead to a detachment of the joints. The goal is to place the thermocouples as close as possible to the deposited wall, but still gain significant data. A PCE-T 390 multichannel digital thermometer is used to read and store the thermocouple signals. Temperature is recorded with a sampling frequency of 1 Hz.

(a)

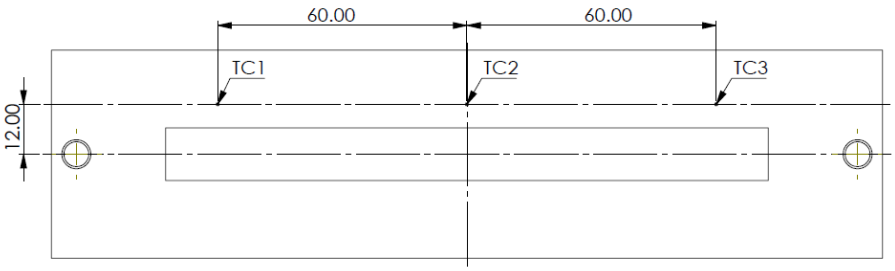

(b)

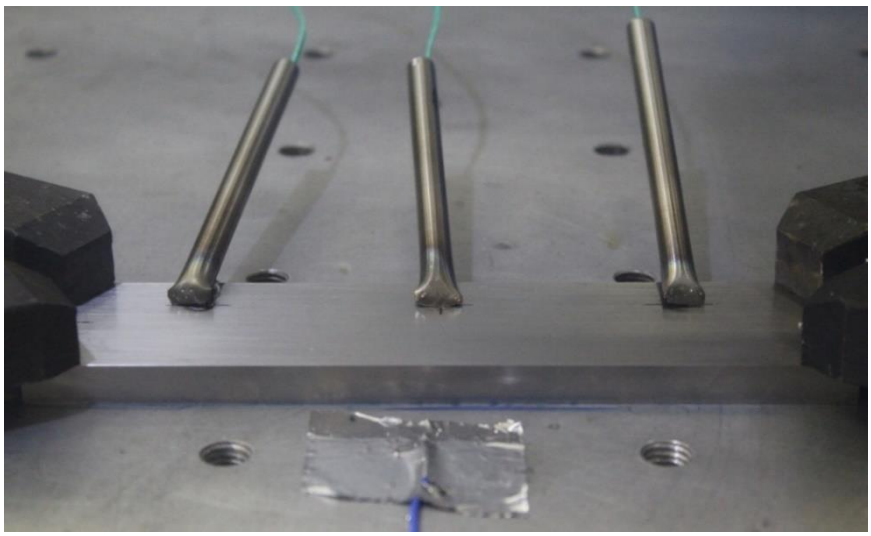

Fig. 3 (a) Schematic view of the thermocouple locations on the top surface of the baseplate; (b) Steel pipes protecting the thermocouples from the plasma

Additional PCE TF-500 type K thermocouples are installed to capture the temperature of the backing plate, the clamps and the ambient inside the welding chamber. The thermocouple data are processed in MATLAB R2016a to determine temperature profiles of the plasma metal deposition process. The temperature history is further used to validate the numerical model in Simufact Welding 8.0.

POST-PROCESS DISTORTION MEASUREMENTS

Distortion is defined as the changes in the dimensions and the shape of a workpiece. Dimensional and shape changes can occur individually, but are usually superimposed. To obtain distortions imposed by the PMD process, the pre- and post-process profiles of the baseplates are scanned utilising a coordinate measuring machine (CMM). Measurements with a HEXAGON m&h IRP40.02 infrared touch probe system with a 1 mm ruby stylus

are performed along the top and bottom surfaces of the baseplates. The measurement grid on the top surface consists of 40 points, whereas the measurement grid on the bottom surface consists of 45 points, respectively. The locations at both surfaces are identified in Fig. 4.

(a)

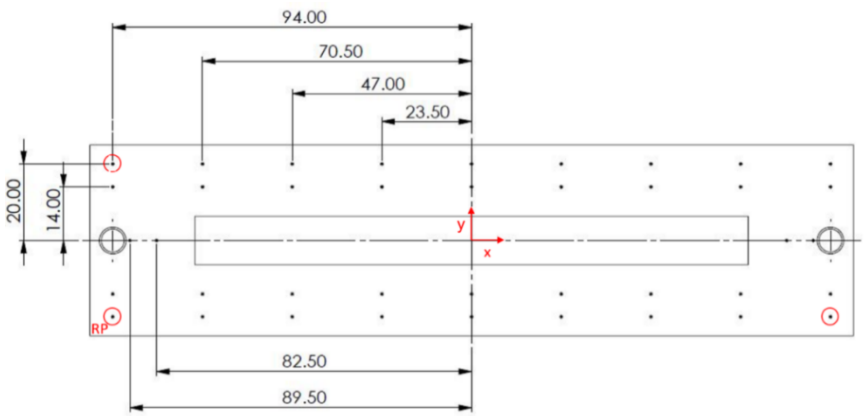

(b)

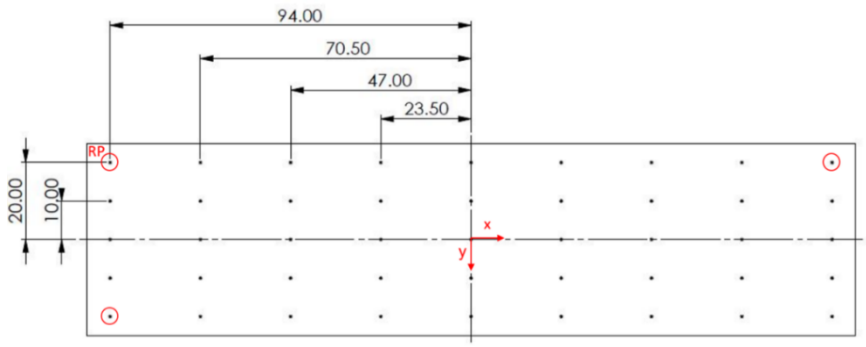

Fig. 4 Schematic view of CMM points on the (a) top surface, and (b) bottom surface of the baseplate

The bottom surface is scanned with a 9x5 measurement grid, with a grid spacing of 23.5 mm in x and 10 mm in y direction. A different strategy is adopted for the top surface, since the single bead wall and the two blind holes do not allow a constant grid spacing. Hence, a measurement grid of 40 points in total is defined for the top surface. A reference plane with the points marked in red is constructed for each surface to align the coordinate frames of both surfaces. Rigid body translation and rotation is applied to make these planes parallel to the xy-plane. Additionally, a reference point (RP) is defined as centre of rotation. The results from the discrete data points are then used to calculate the changes in plate profile and out-of-plane distortion by subtracting the pre-process from the post-process measurements. For reasons of symmetry, sampling lines along the

longitudinal direction with symmetric y-values are merged to one single line and their mean values and standard deviations are calculated. This results in effective sampling lines for y=0 mm, y=14 mm and y=20 mm for the top surface and y=0 mm, y=10 mm, y=20 mm for the bottom surface, respectively. The experimentally determined distortion is used to evaluate the simulation results obtained by Simufact Welding 8.0. Since the building strategy causes a symmetry break along the transverse direction, this analysis method is not applicable for the transverse direction.

SIMULATION SET-UP

The process simulation of the PMD process to predict the temperature distribution in the component as well as the resulting distortion and residual stresses is set-up within Simufact Welding 8.0. Simufact Welding software covers different welding processes and encompasses the modelling of elastic-plastic behaviour of materials and structural welding simulation. The current release, Simufact Welding 2021, already includes a direct energy deposition tool [10]. The thermal analysis of the WAAM process involves the solution of a heat transfer problem with a moving heat source. Since 1984, the most widely used model in computational welding mechanics has been the power density distribution function with net weld power and weld pool shape, size and position as a function of time introduced by Goldak et al. [9] for the simulation of welding processes. Within the arc welding module, Simufact Welding 8.0 employs the Goldak double ellipsoid as standard heat source (Fig. 5). The moving double ellipsoid model can describe a wide variety of welding techniques, including gas metal arc welding, gas tungsten arc welding, shielded metal arc welding and submerged arc welding [11].

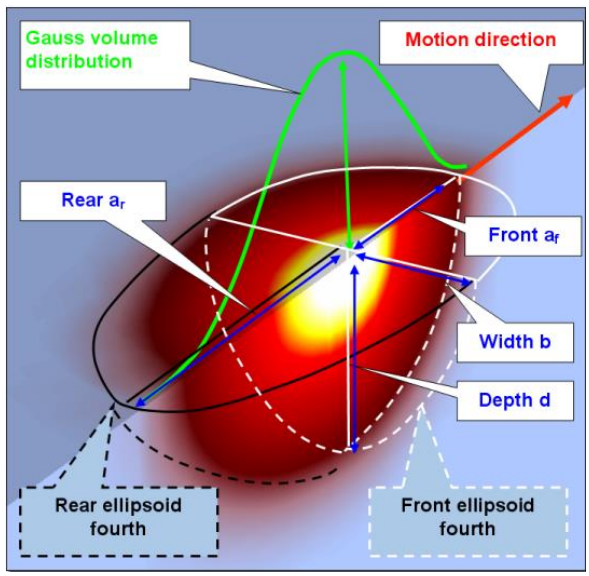

Fig. 5 Illustration of Goldak's double ellipsoid heat source model [11]

Inputs for Goldak's double ellipsoid heat source model include the calibration of six parameters a_f, a_r, b, d, M and η to calibrate the heat source model [11]. The heat source parameters have been determined in a previous study and are listed in Table 3.

Table 3 Goldak double ellipsoid heat source parameters

Run	a_f [mm]	a_r [mm]	b [mm]	d [mm]	M [-]	f_f [-]
Preheating	2.85	5.70	2.85	1.4	0	0.66
Deposition	6.72	13.44	6.72	4.41	0	0.66

The cooling behaviour and arc efficiency are determined by inverse simulation. From this, an arc efficiency of 0.4, an emissivity of 0.7, a convective heat transfer coefficient of 8 W/(m²·K) and a contact heat transfer coefficient of 10 W/(m²·K) are obtained. The parameters for the thermal boundary conditions are assumed to be independent of the temperature. A summary of the welding parameters used for the simulation is presented in Table 4.

Table 4 Welding parameters

Run	I [A]	U [V]	v_{TS} [mm/min]	η [-]	E_l [J/mm]
Preheating	130	25	300	0.4	260
Deposition	140	25	200	0.4	420

MATERIAL DEPOSITION MODELLING

Plasma metal deposition can be related to a multi-layer welding process, in which the filler material is melted and deposited layer-by-layer. The deposition of the melted material along the welding path has to be implemented in the physics based finite element framework of the additive manufacturing process. Depending on the finite element activation/deactivation technique, the filler material can be simulated in two ways: the quiet element method or the inactive element method [12], [13]. The quiet element method is based on the initial existence of all elements in the model, i.e., all elements of the mesh defining the baseplate and successive layers to be deposited are included in the initial computational model. These elements are made passive (quiet) by multiplying material properties by scaling factors which do not affect the rest of the model. As material is deposited, the real thermo-physical properties are re-established based on the location of the energy source switching the elements to active. In this study, the quiet element method is used. The second approach removes elements representing material to be deposited from the computational analysis up to their activation. According to the metal deposition along the welding path, elements are switched to active and assembled into the model. Thus, only the mesh representing the base material and already deposited layers are computed and assembled into the global matrix. Michaleris [14] developed a hybrid quiet/inactive element method accelerating computer run times. Hereby, elements corresponding to material deposition are initially inactive and elements of the current deposited layer are switched to quiet. Based on the location of the energy source, quiet

elements are switched to active as material is deposited. This approach is implemented in Simufact Welding 2021.

Within Simufact Welding, the welding process is designed based upon manufacturing data: welding process, energy input, welding speed, filler material, welding metallurgy, clamping concept, components and the finite element mesh have to be defined. All components have been designed in SoildWorks 2018 and meshed in Abaqus CAE 6.14. Symmetry properties are exploited by modelling only one half of the calibration setup. This significantly reduces calculation time. To determine the cross-section profiles of the fabricated Ti-6Al-4V walls, demonstrator 3 is exemplary cut in two halves using WEDM. The cut surface of one half is then scanned with an Alicona Infinite Focus optical 3D measurement system. The 3D point cloud obtained is analysed and edited in MATLAB 2016a. From the three-dimensional data points, a two-dimensional projection of the cut surface is computed. Points defining the boundary of the surface are determined and exported to SolidWorks 2018. Within the CAD software, the imported pointes are connected using spline interpolation to reconstruct the cross section of demonstrator 3. The 2D surface scan of the cross section and the reconstructed cross section are shown in Fig. 6.

(a) *(b)*

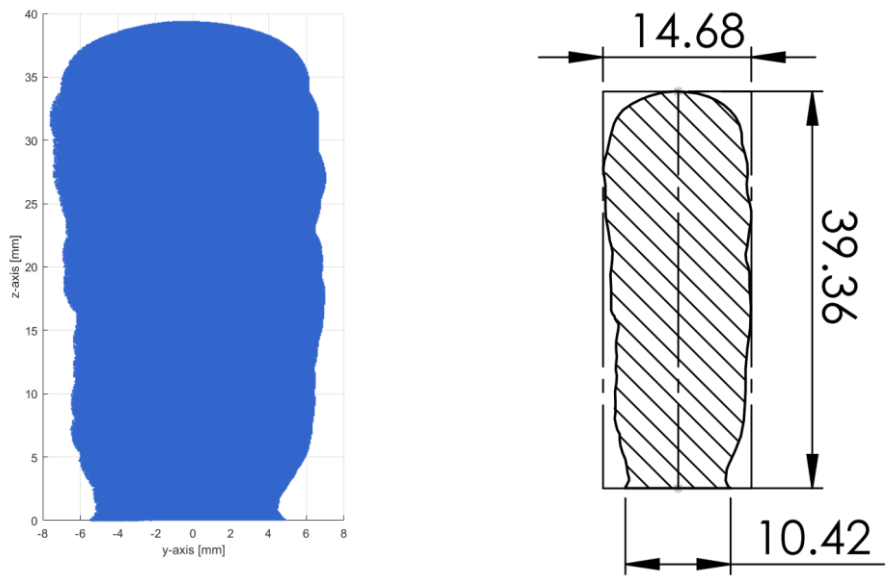

Fig. 6 (a) Point cloud derived in MATLAB; (b) Derived CAD model within SolidWorks

In this study, each welding seam is considered as rectangular cross section. This approach reduces model complexity and enables engineers to set up simulations faster. For components with more complex geometries, the implementation of detailed weld beads increases the modelling effort. Moreover, the exact geometry of the weld beads is not always known. Some numerical studies considered each welding seam as rectangular cross section yielding good results [4], [15]. To determine the rectangular cross-section

profiles, area and height of the wall are divided by the total number of deposited layers. The dimensions used for the determination of the rectangular layer geometry are summarised in Table 5.

Table 5 Cross-sectional dimensions of demonstrator 3

Total area [mm²]	Total wall height [mm]	Number of layers [-]
498.15	39.36	32

From Table 5, the cross-sectional area and layer height for each deposited layer are determined as 15.6 mm² and 1.2 mm, respectively. The wall width of each layer is the result of the cross-sectional area divided by the layer height yielding 12.7 mm. An overview of the layer geometry is presented in Table 6.

Table 6 Layer dimensions

CSA [mm²]	Layer height [mm]	Wall width [mm]
15.6	1.2	12.7

With these parameters, the 3D model of the deposited wall is reconstructed in a layer-wise fashion. A model view of the plasma metal deposition process is shown in Fig. 7.

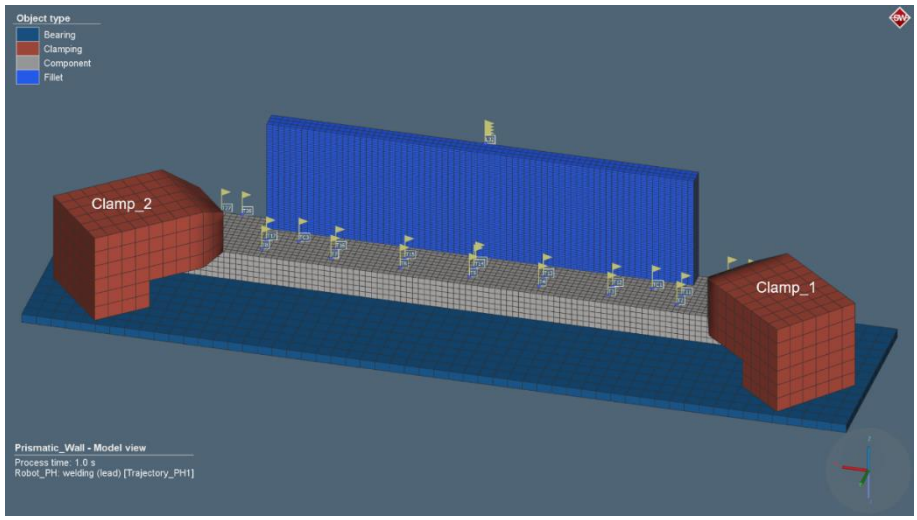

Fig. 7 Half-symmetry model of the PMD process

The backing plate is modelled as a bearing. This type of boundary condition enables separation and sliding of components in contact with the bearing and prevents nodes of components in contact with the bearing from movement into the bearing. The clamping concept of the deposition experiments is implemented in the simulation using simplified models of the clamps. In Simufact Welding, clamps work as springs applying a force opposite to a movement normal to the surface depending on the size of the displacements.

Additionally, clamps are pressing components against each other. The clamping movement is controlled via a stiffness and a force. The stiffness is estimated 3,837 N/mm and the clamping force 67,6 N as outlined in the "Appendices". The estimation of these parameters has been performed in Abaqus CAE6.14 using the finite element approach. For the plasma metal deposition model, linear hexahedral elements with eight integration points are used for the thermo-mechanical simulation. The baseplate and the layers are meshed with a global element size of 2 mm, the backing plate and the clamps with a global element size of 5 mm. Each layer is additionally seeded with two elements over the layer height. The overall mesh consists of a total number of 21,820 elements and total number of 39,406 nodes. To trace result values at certain positions in the model, particles are defined at coordinates corresponding to the measurement grid used for the distortion measurements and to the thermocouple locations. In addition, particles are placed along the geometric centreline of the wall ranging from the bottom of the baseplate to the top layer. The results of the tracking points are used to compare the numerical data with the experiments.

Within the robot menu in Simufact Welding, different timings of the welding process can be adjusted. This enables a close to reality integration of sequences of the welding process from the G-code directly into the simulation. The exact timings for preheating and layer deposition are shown in Fig. 8.

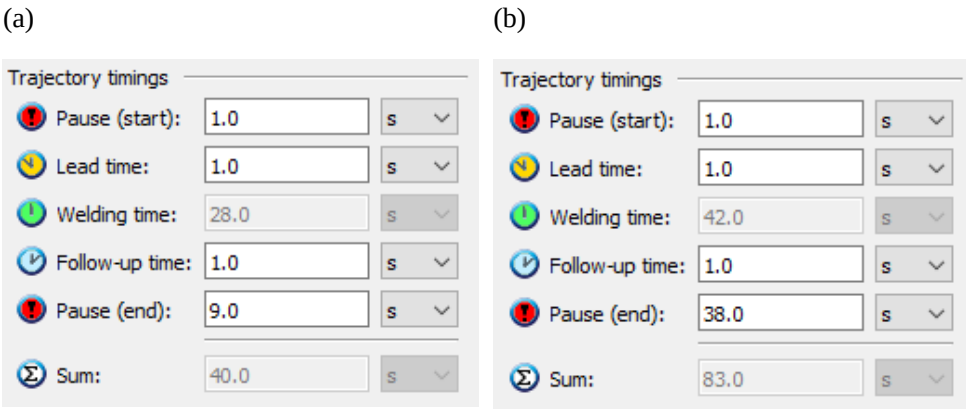

Fig. 8 Trajectory timings: (a) Preheating; (b) Deposition

The pause time in the beginning considers a delay time to purge locally with argon (no energy input), while the lead time considers a delay with an active heat source to melt the material at the start point. Within the lead time, the feed of the wire is initiated. During the first two sequences, there is no movement of the heat source. The welding time is automatically calculated by Simufact Welding as the quotient of trajectory length and welding speed. At the end of the trajectory, the movement stops, but the heat source is still active. This time period is called follow-up time. The cooling time between layers for preheating and printing is set to 1 s and 30 s, respectively, which yield, together with the travel movements of the gantry to the park position, a total dwell time of 9 s and 38 s between subsequent layers (no energy input).

Based on the experimental trials, the time frame for depositing the walls and cooling down to room temperature is known. As a result, the total simulation time is set to 4,000 s. To investigate the behaviour of the wall upon clamp release, the model is computed using three different strategies for unclamping. Fig. 9 schematically shows the individual clamp release times.

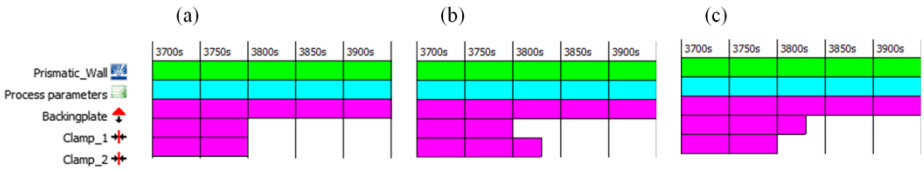

Fig. 9 Process control centre indicating clamp release times: (a) Simultaneous unclamping; (b) Clamp 1 followed by clamp 2; (c) Clamp 2 followed by clamp 1

The delay time for non-simultaneous release of clamp 1 and clamp 2 and vice versa is set to 30 s. This time interval approximately corresponds to manual release of the clamps after the deposition process.

AEROSPACE BRACKET MODEL

Finally, a common connecting element or fastening element in the aerospace industry is analysed. Aircraft brackets are essentially supported structures that are used to attach two different components while supporting one over the other. Redesigning brackets for AM can result in significant reduction of material costs, reduced mechanical post processing, weight savings and can decrease fuel consumption of airplanes. The 3D model of the to-built geometry and the part after machining are schematically shown in Fig. 10.

(a) (b)

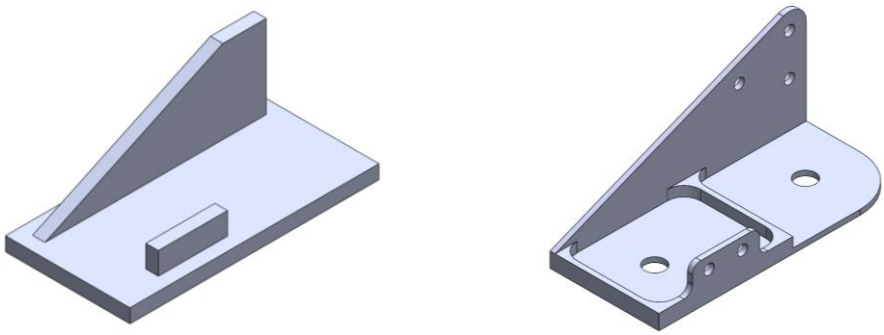

Fig. 10 3D model of the bracket in the (a) as-built condition and (b) after final machining

Fig. 10 (a) shows that the to-be-built geometry is oversized in order to incorporate the final geometry and to take into account the material loss due to mechanical postprocessing. From this CAD file, the building strategy for the PMD process is derived. The part consists of two single walls deposited on a rectangular Ti-6Al-4V baseplate. The walls are built up layer by layer until a pre-defined height is reached. The goal is to determine the optimal building strategy by using numerical simulations to minimise distortion and reduce residual stresses. Two building strategies are investigated: firstly, the small wall is deposited followed by the subsequent deposition of the inclined wall and, secondly, a layer of the small wall is followed by a layer of the inclined wall. Both strategies are based on bidirectional layer deposition. The baseplate is fixed to the backing plate of the welding chamber with two clamps. Prior to deposition, the cold baseplate is preheated with the arc to improve bonding of the first layers to the baseplate. A model view of the bracket is shown in Fig. 11. The set-up allows no exploitation of symmetry properties.

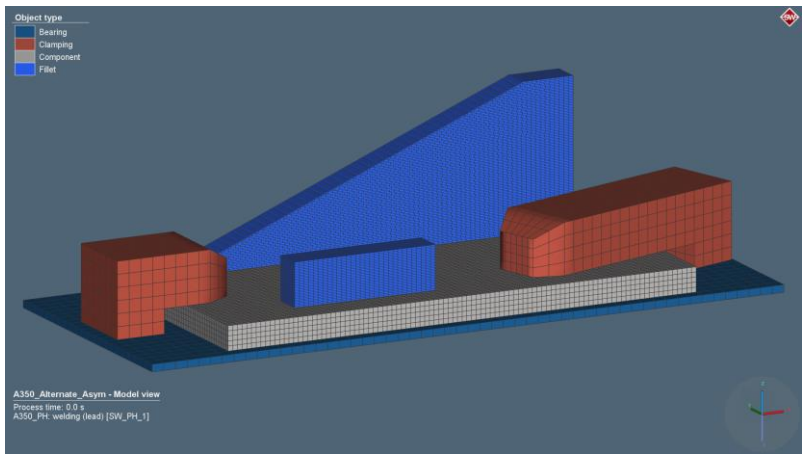

Fig. 11 Model view of the airplane bracket

Linear hexahedral elements with eight integration points are used for the thermo-mechanical simulation. The baseplate and the walls are meshed with a global element size of 2 mm, the backing plate and the clamps with a global element size of 5 mm. Each layer is additionally seeded with two elements over the layer height. The overall mesh consists of a total number of 61,612 elements and total number of 96,450 nodes. The deposition parameters for the fabrication of the bracket correspond to the parameters utilised for the additive manufacturing of the single wall structures listed in Table 4. The dwell time between layers is estimated with 6 s, which corresponds to the time needed for the gantry to travel from the end position of the current layer to the start position of the subsequent layer. The total simulation time is set to 3,600 s. Clamps are released simultaneously after 3,540 s. Accordingly, the results achieved are used to elaborate an optimal building strategy for the process to demonstrate the practicability of numerical simulations on an industrial scale.

RESULTS

Ti-6Al-4V single wall structures

A series of eight single wall structures is fabricated using a plasma-based direct energy deposition process. As material of interest, an α/β titanium alloy (Ti-6Al-4V) is investigated. Multi-layer walls are deposited along the centreline of the baseplate with reversed welding directions for each layer. Each wall consists of 32 layers. Average wall height and average maximum wall width have been measured at the centre of the deposited walls and are 37.5 ± 1.0 mm and 13.3 ± 0.5 mm, respectively. The average mass of the single wall structures is 300 ± 11 g. The total layer height divided by the number of layers yields an average layer height of 1.2 ± 0.1 mm. An example of a Ti-6Al-4V wall built by plasma metal deposition is shown in Fig. 12.

(a)

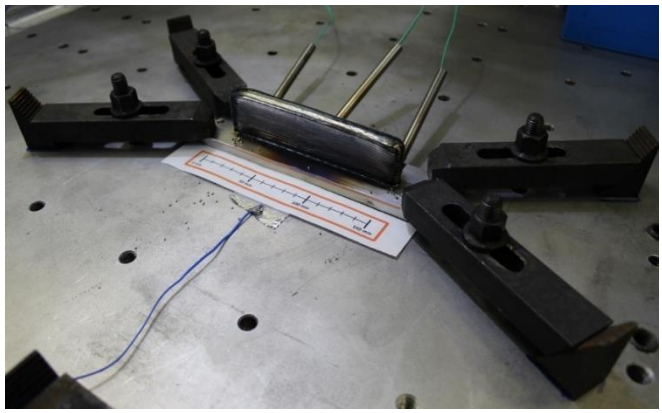

(b)

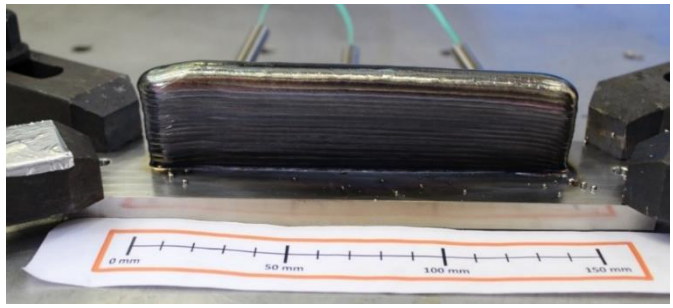

Fig. 12 Ti-6Al-4V single wall structure produced with plasma metal deposition

All demonstrators have a silver colour which is a sign of proper shielding against atmospheric contamination. The surface discoloration of Ti-6Al-4V can be used to visually assess the degree of oxidation. With increasing oxidation, the surface colour changes from metallic silver, light straw through dark straw, light blue, dark blue, to grey and powdery [16]. Further visual assessment reveals an increase in wall width along the build height. This observation is also confirmed by measurements of the layer height and wall width during deposition. The layer height and the maximum wall width (considering the surface waviness of the weld) are measured with a calliper after the 10th, 20th and 32nd layer at the centre of the wall. Since manual recording of measurement data inside the welding chamber is quite laborious and, in order not to interrupt the continuity of the process, measurements are only conducted at a few points. The layer height and wall width along the build height can be seen in Fig. 13.

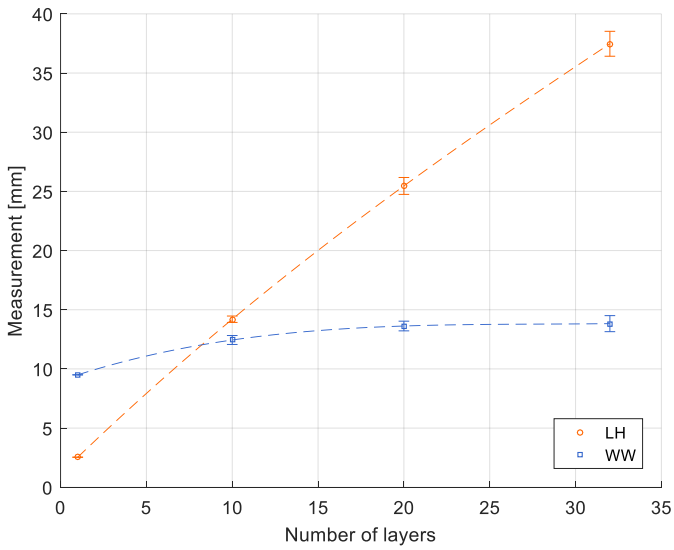

Fig. 13 Layer height and wall width measured during deposition

Fig. 13 shows that the layer height increases nearly linearly with increasing wall height. The width of the cross section, on the contrary, experiences a steady increase from the first layer, reaching a steady deposition width at higher layers. This geometry-related phenomenon can be explained by the balance of heat input and dissipation. In the first few layers, the thermal effect of the baseplate leads to a reduction in wall width (WW) and an increase in layer height (LH). This effect has been observed by Martina et al. [2], [7] and described by Wu et al. [16]. The thermal history of WAAM components is governed by a balance between conduction, convection, and radiation. As reported by Wu et al. [16], the cold baseplate acts as a heat sink in the first layers, leading to faster cooling rates and, thus, narrower beads. Convection and radiation become more significant with the component being built up layer by layer. With an increasing wall height, the conductive thermal resistance to the baseplate, which heats up during the deposition process, is increased. Despite titanium being a poor thermal conductor, convection and radiation are less effective than conduction. The molten pool dissipates heat at slower rates and, therefore, wider beads can be observed with increasing wall height until the heat dissipation and heat input reach a balance resulting in steady wall widths. For a more precise evaluation, additional measurement data are required. The results shown, however, reflect the balance of energy input and dissipation as a geometrical boundary condition well and give insight into the development of the cross sections of deposited walls at constant deposition parameters. To achieve consistent geometrical dimensions, i.e., WW and LH, throughout the whole AM process, the building strategy must be adopted accordingly. For the sake of simplicity, all layers have been built with the same set of parameters and consistent building strategy. Single wall model

Thermal

The numerical model for the plasma metal deposition of the single wall structures employs the double ellipsoid heat sources for preheating and depositing obtained from the calibration procedure. The parameters for the thermal boundary conditions are maintained except for the contact heat transfer coefficient. The baseplate is now in contact with the aluminium backing plate. The contact heat loss through the backing plate is determined by running a series of numerical trials and tuning the values such that the predicted temperature profiles match the experimental results. A value of 100 $W/(m^2 \cdot K)$ gives the best match with the experiments. Fig. 14 presents the experimentally measured and numerically obtained temperature profiles during deposition and cooling.

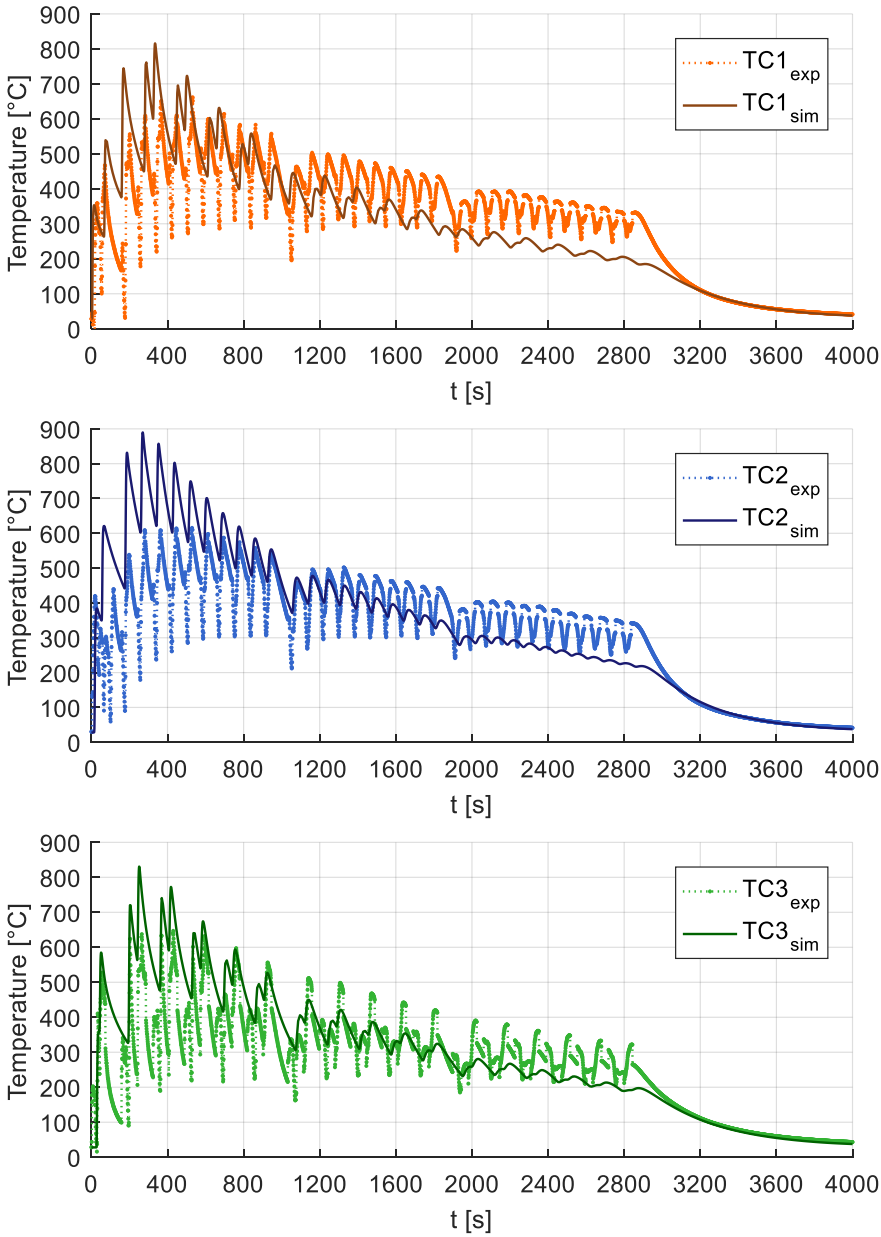

Fig. 14 Temperature profiles obtained during single wall deposition

The overall trend of the temperature evolution is well reflected by the simulation. Referring to the calibration procedures, the peak temperatures in the first layers are overestimated. Over the building time, the thermal profiles of the experiment show a less pronounced temperature decrease than the numerical results. A figurative reason is

believed to be the pilot arc. During dwell times between layers, the torch travels to its park position with the pilot arc active, thus affecting the cooling behaviour of the deposited wall. The initially assumed free convection is locally disturbed by the hot plasma streams of the pilot. Considering the trajectory timings defined in Simufact Welding for the welding process (see Fig. 8), no energy input is defined during the pause time after the end of a trajectory. The cooling curve after the deposition process, however, is well reflected by the simulation indicating that the parameters set for the thermal boundary conditions are accurate. Further, a distinct noise in the experimental measurement signal can be noticed. This may be due to insufficient shielding of the thermocouple against the electromagnetic influence of the plasma.

Mechanical

The mechanical behavior of the additively manufactured walls is investigated. The total distortion is an important evaluation index of plasma metal deposited components. Distortion has a strong impact on the dimensional precision. Fig. 15 displays measured and numerical post process displacements along the longitudinal direction after cooling and under different cases of unclamping. The course of the displacements between the data points has been modelled using spline interpolation. In the case for y=0 mm at the top surface, no data points along the wall are available. Thus, the interpolation between the four remaining points, (x=-89.5 mm, x=-82.5 mm and x=82.5 mm, x=89.5 mm, respectively) serves only as an indicator for the gradient in the out-of-plane distortion between these points and cannot be compared with the other measurement lines at the top surface.

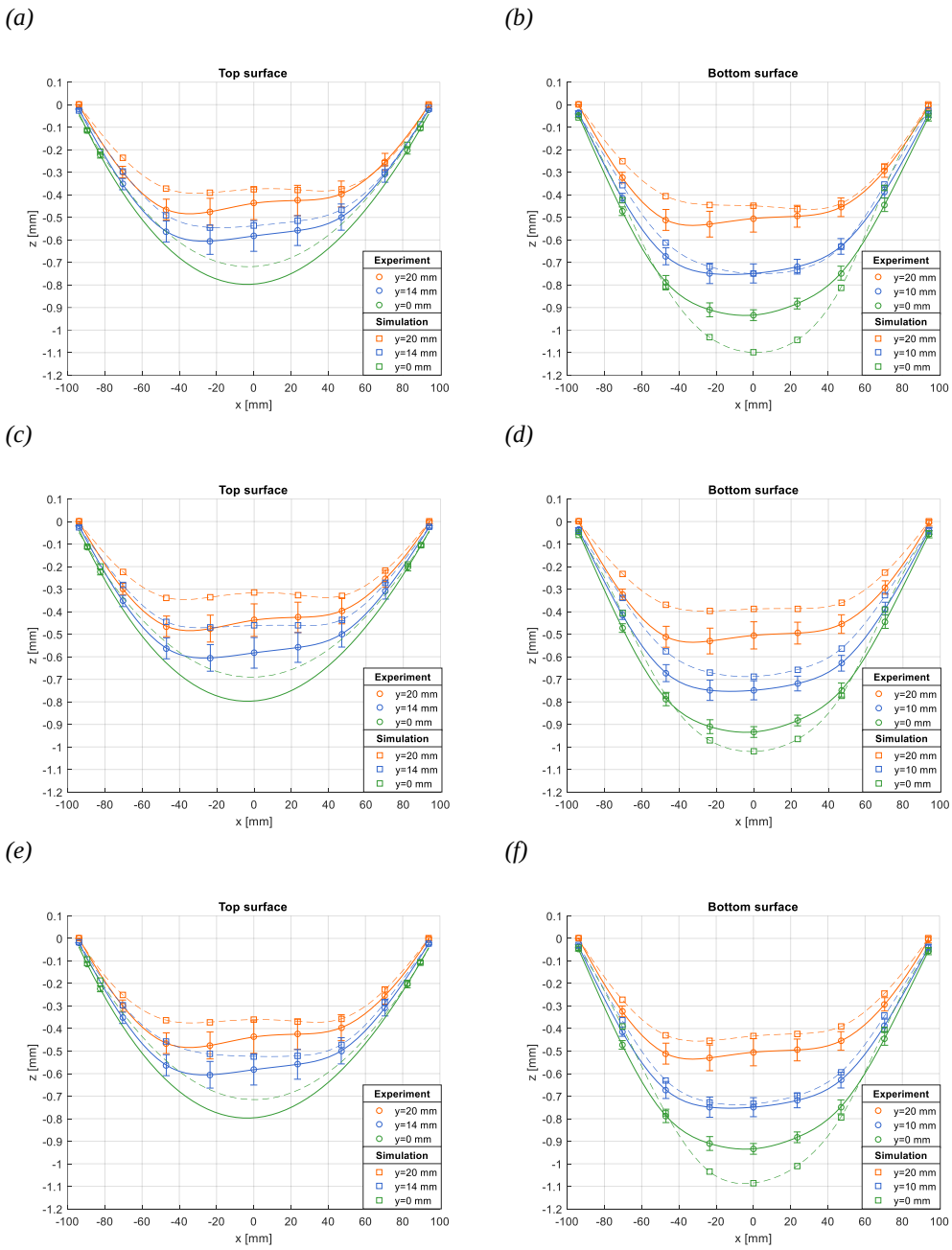

Fig. 15 Out-of-plane distortion along the longitudinal direction: (a) and (b) clamp 1 followed by clamp 2; (c) and (d) simultaneous unclamping; (e) and (f) clamp 2 followed by clamp 1

The predicted distortions of all three unclamping cases are compared to the measured distortion. In Fig. 15, the downward bending of the baseplate in relation to the reference

plane defined in “Post-process distortion measurements” can be seen. It should be noted that, in recent studies, the authors refer to this phenomenon as upward bending, as it is a matter of reference. To stay consistent with their terminology, upward bending is further used in this paper. The upward bending can be explained as follows [5]: the deposited layer expands during heating and contracts during cooling. The contraction of the upper layer is constrained by the previously deposited layers and generates tensile residual stress, resulting in upward bending of the baseplate. Larger distortions are found at the bottom surface. Here, the baseplate bends upwards by approximately 0.9 mm at the centreline of the surface showing the maximum distortion. Comparing the scan lines at y=10 mm and y=14 mm, the top surface shows a less pronounced out-of-plane distortion. The scan lines at y=20 mm show similar values at both surfaces. Another prominent observation from the measured data points is their asymmetrical course over the length of the baseplate. Although a bidirectional building strategy is employed, already the deposition of the first layer causes non-uniform heating and cooling of the baseplate. As a result of the non-homogenous temperature field, non-uniform thermal expansion of the heat affected zone leads to a non-homogenous plastic deformation, triggering the asymmetric behaviour of the baseplate. Although all eight demonstrators are built with the same process parameters, the CMM points are subject to a certain range of fluctuation. Deviations in the application of the clamping forces, a modified temperature control, influence of the rolling direction of the baseplates, the geometry of the wall - all these factors impact the final distortion of each component.

A graphical evaluation of Fig. 15 reveals a qualitative agreement of the modelling results with the measurements, despite representing noticeable smaller deflections. The only exception is the longitudinal distortion along the centreline of the baseplate at y=0 mm of the bottom surface. Here, the numerical results overpredict the distortion. The deviations between experimental and numerical values are strongly linked to the heat input and the mechanical and thermal boundary conditions. Referring to the temperature history plot in Fig. 14, the temperature profiles obtained from the simulation decrease at a higher rate over the building time resulting in faster cooling than the experimentally measured profiles. This in turn leads to the material being stiffer, yielding smaller displacements. In the simulation, it is also assumed that the backing plate is rigid and does not allow any penetration of the baseplate. In reality, of course, the aluminium backing plate has a lower stiffness than the titanium baseplate and tends to deform locally elastically and plastically due to mechanical clamping forces exerted on the Ti-6Al-4V baseplate. All these factors are linked to the evolution of the final distortion of the PMD single wall structure. In each of the cases in Fig. 15, the numerical results display a similar accumulation of distortion after cooling and unclamping. The case of simultaneous unclamping follows the course of the CMM points for the top and bottom surface most precisely, but shows a high deviation in the residuals. On the contrary, Fig. 15 (a), case 1 top surface, approximates the out-of-plane distortion of the top surface best, while Fig. 15 (f), case 3 bottom surface, appears to fit the data of the bottom surface best. Error metrics from statistics are used to judge the quality of the models and verify the statements above. The mean absolute percentage error (MAPE) for each case can be calculated as

$$\mathrm{MAPE} = \frac{100\%}{n}\sum_{i=1}^{n}\left|\frac{x_i^{\exp}-x_i^{\mathrm{sim}}}{x_i^{\exp}}\right| \quad (1)$$

where n is the total number of data points, i the current data point, $x^{\exp}$ is the experimental value and x^{sim} is the simulated value. Table 7 shows the mean absolute percentage error for the top and bottom surface for all three unclamping cases.

Table 7 MAPE for the unclamping cases

Case	Description	MAPE top surface [%]	MAPE bottom surface [%]
1	Clamp 1 followed by clamp 2	12.60	12.57
2	Simultaneous unclamping	15.33	15.23
3	Clamp 2 followed by clamp 1	11.96	11.16

A good correlation is achieved for each case fitting the top and bottom surface in equal measure. Thus, each unclamping strategy is, within numerical and experimental errors, suitable to predict the out-of-plane distortion of the PMD single wall structure. The largest errors are found for symmetric unclamping, while case 3 (clamp 2 follows clamp 1) shows the lowest errors for both, the top and bottom surface. The most prominent observation from these numbers, though, appears to be that the prediction of the out-of-plane distortion of the bottom surface is more accurate than the prediction of the top surface, i.e., the MAPE value of the bottom surface is smaller than the MAPE value of the top surface. Contrary to the expectation that Fig. 15 (a) matches the top surface and Fig. 15 (f) matches the bottom surface best, the unclamping strategy of case 3 fits according to the MAPE values the measured distortion most accurately. It becomes evident that different unclamping strategies affect the final distortion of the PMD walls. Fig. 16 (a) and (b) illustrate the predicted total displacement of the wall after case 3 cooling and unclamping. The distortion of the model is scaled by a factor of 4 so that the deformation becomes evident and to emphasise the deformation of the baseplate.

(a)

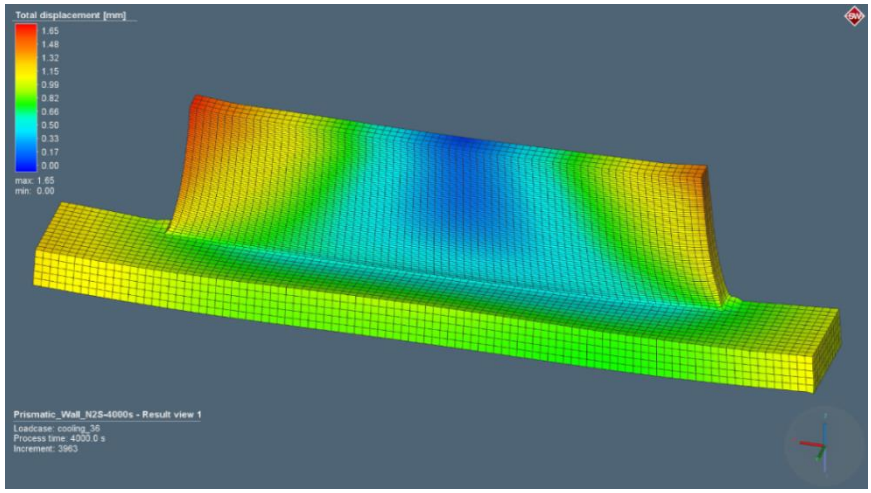

(b)

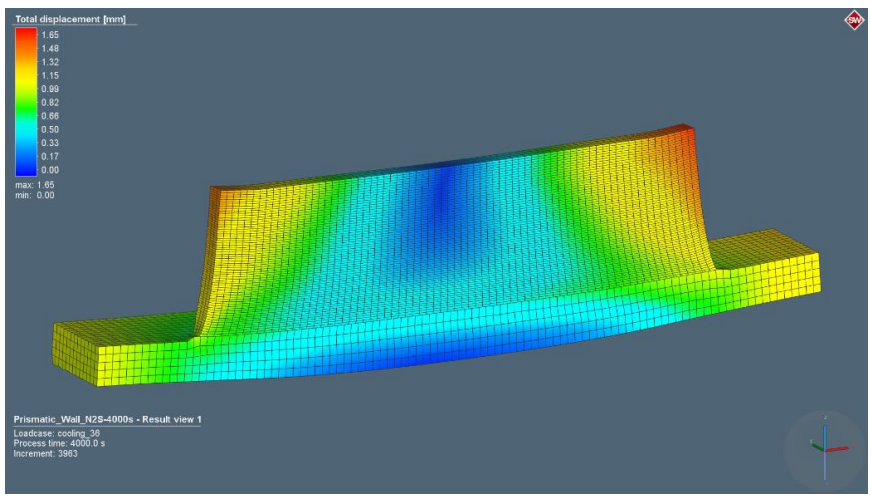

Fig. 16 Total displacement of the PMD wall after case 3 cooling and unclamping: (a) Overview; (b) Symmetry plane

After unclamping and cooling, the component bends upwards and shows significant out-of-plane distortion. The deposition of liquid metal on a solid baseplate and its constrained shrinkage during cooling causes elastic and plastic deformations. In the central area of the wall, distortion is restricted due to the wall itself functioning as a stiffening structure. At the bottom, distortion is restricted by the backing plate. The deposited wall is pulling the baseplate upwards causing a significant residual stress state. The mean normal stress, which is the average of the three principal stresses, for case 3 cooling and unclamping is shown in Fig. 17. The mean normal stress of the model is scaled by a factor of 4.

(a)

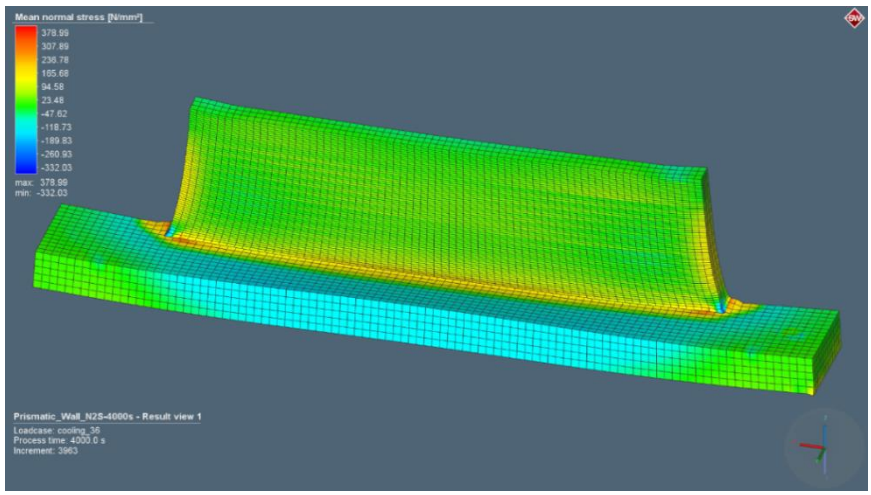

(b)

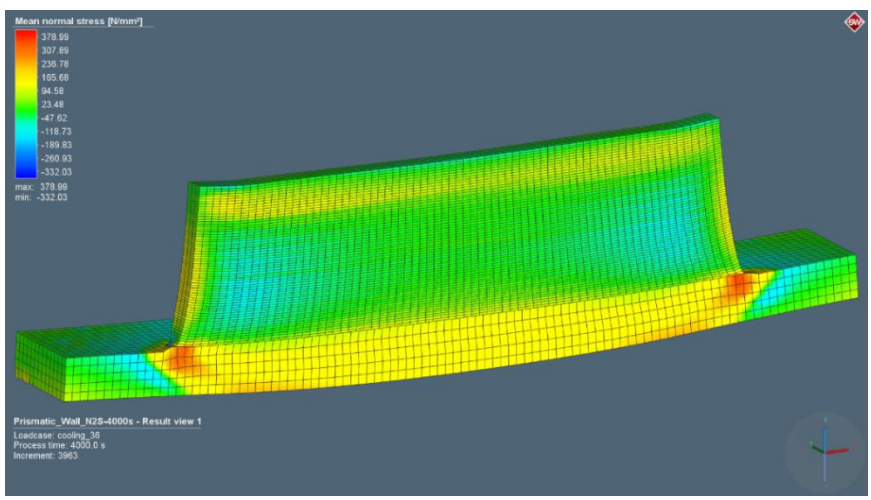

Fig. 17 Mean normal stress of the PMD wall after case 3 cooling and unclamping: (a) Overview; (b) Symmetry plane

In Simufact Welding 8.0, the residual stress distribution can be analysed. Most areas of the component are subjected to tensile residual stresses. Compressive stresses occur in the baseplate in an area surrounding the deposited wall and in the mid-outer regions of the wall. Another interesting observation is the stress concentration at the bonding area of the wall to the baseplate. Here, tensile residual stresses reach a maximum making this critical point susceptible to cracking and delamination. Such stress concentrations can be identified by the simulation and incorporated into strategies to avoid tearing or delamination of the deposited material. Due to thermal effects inherent to plasma metal deposition, in-process and post-process distortion and residual stresses are unavoidable.

Dimensional and shape changes can be used to identify the effects of resulting residual stresses. The residual stress distribution along the centreline of the additive manufactured wall before and after releasing the mechanical boundary conditions can be seen in Fig. 18.

(a) (b)

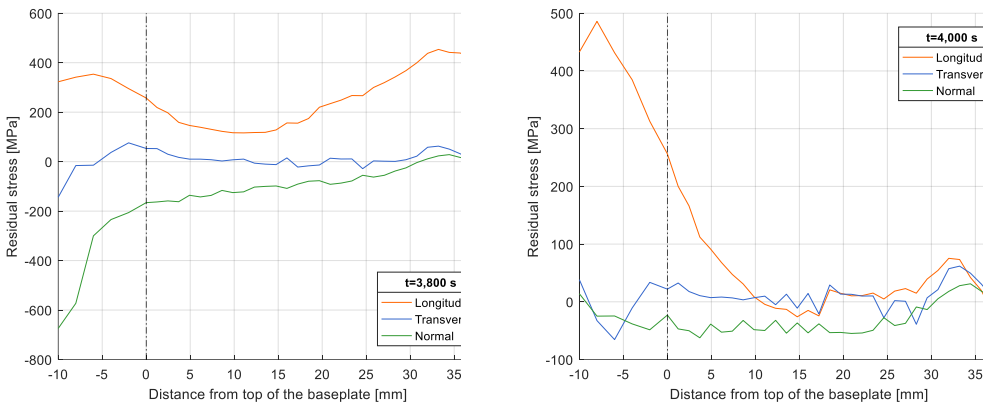

Fig. 18 Predicted residual stress along the centreline of the wall in longitudinal (x), transverse (y), and normal (z) direction while: (a) clamps are on; (b) clamps are off

When the specimen is clamped, the longitudinal stress predicted across the wall shows first a local peak in the baseplate and then starts to decrease until a wall height of around 15 mm is reached. The stress in the first layers of the deposit is relatively uniform. Towards the final build height, the stress is increasing, reaching its highest value in the deposited wall. The transverse stress is ranging from -140 MPa to 75 MPa and is significantly lower than the longitudinal stresses. Normal stress shows a high accumulation of compressive stress in the baseplate and is steadily increasing over the build height of the wall. Upon releasing the clamps, stress relaxation occurs and inherent plastic strains cause the specimen to bend upwards. Distortion changes the stress field by reducing the tensile stresses in the top of the wall and by increasing tensile stresses in the bottom of the baseplate. The interesting aspect of the longitudinal stresses in Fig. 15 (b) occurs towards the extremities of the wall. For example, the stress at the top of the wall has a much lower value than at the bottom of the baseplate due to the distortion of the component. This distortion also causes the stress at the bottom of the plate to become highly tensile. There is a reduction of the tensile longitudinal stresses from the baseplate with an increased number of layers. Within a wall height of 10 mm to 30 mm, longitudinal and transverse stresses are almost zero, reaching a peak between 30 mm and 35 mm and are becoming compressive at the top of the wall. Interestingly, there are no significant jumps in the stress profiles at the baseplate-wall interface, as several studies reported [4], [5], [7], [17]. The difference is found to be in the clamping strategy. In this work, the baseplate has been clamped only at its four corners allowing the material to distort in the central area during the process. In Refs. [4], [5], [7], [17], a more thorough clamping restricting the movement of the baseplate is used. Investigations showed that uniform residual stresses are produced along the wall during the process being balanced

by compressive stresses in the baseplate with a non-continuous transition at the interface. Unclamping causes a redistribution of the stresses. Tensile stresses drop linearly towards the top of the wall. Colegrove et al. [5] proposed an analytical model to estimate the residual stress in the longitudinal direction. One assumption of this model is that there is no deflection of the component during deposition. Hönnige et al. [18] used the analytical model for estimating distortion and residual stress with reasonably good accuracy. It should be noted that the stress profiles in Fig. 18 are determined numerically and need, of course, experimental validation. However, the numerically obtained stress profiles are in good correlation with works conducted by Martina et al. [7] and Hoye et al. [17] showing a similar distribution of stress within an additively manufactured wall structure.

AEROSPACE BRACKET MODEL

Manufacturing of complex structures for industrial applications requires innovative software solutions that enable precise, reliable and reproducible predictions of distortion and residuals stress fields. Simple geometries, such as single wall structures, can be used to validate the numerical models and raise confidence in structural welding simulations to simulate more complex parts. Based on this considerations, computer-aided calculations are used to determine the optimal building strategy for the plasma deposition of a Ti-6Al-4V aerospace bracket. Two building strategies have been identified prior to the process, which are analysed virtually. The mechanical performance of both strategies after cooling and unclamping is examined. The total distortion is presented in Fig. 19 scaled by a factor of 4.

(a)

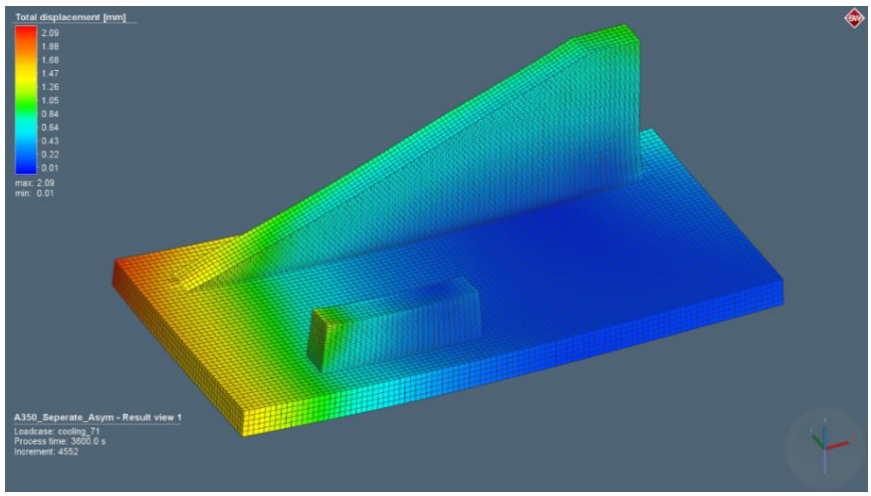

(b)

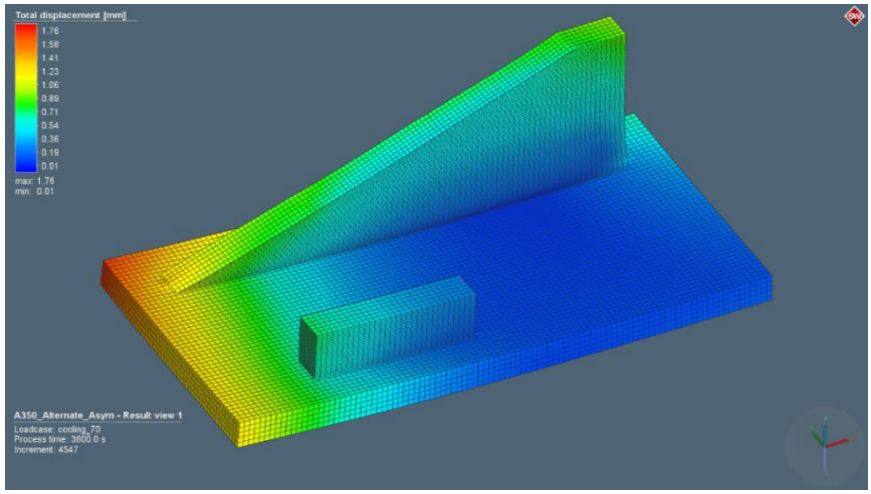

Fig. 19 Total displacement of the aerospace bracket after cooling and unclamping: (a) Strategy 1; (b) Strategy 2

Both building strategies yield similar results regarding the total distortion. Strategy 1, however, shows larger values of distortion in the region where the inclined wall is rising. In this corner, there is no mechanical restraint and the inclined wall is pulling the baseplate upwards. Due to a more homogenous heat distribution of strategy 2, the component is subject to less distortion. Considering the manufacturing of a component on the industrial scale, more attention should be paid to the clamping strategy. To reduce the overall distortion of the bracket, a different clamping strategy would be required. However, due to the dimensions of the baseplate and the design of the plasma torch, the chosen clamping strategy guaranteed accessibility of the torch reaching every start and stop point without crashing.

Numerical simulations are a powerful technique to analyse the thermal and mechanical evolution of components and their properties during the additive manufacturing process. Assessing the results of the numerical simulations, strategy 2 is employed for the additive manufacturing of the Ti-6Al-4V bracket. Less distortion and a more homogenous heat distribution are the driving factors. Fig. 20 shows the bracket in the as-built condition and after final machining.

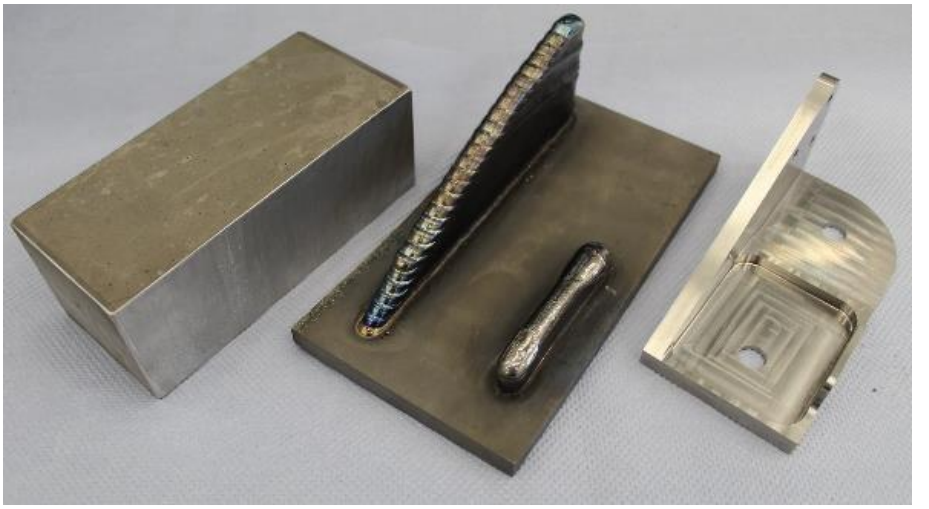

Fig. 20 Aerospace bracket manufacturing

The walls show a homogeneous macrostructure without the occurrence of defects. It can be deduced that PMD can be used to produce large-volume homogeneous parts and components. The advantage for a production by means of additive manufacturing is reflected in the material savings, reduced mechanical post-processing and resulting cost savings. In comparison to conventional production methods, the production by means of generative methods allows material savings up to approximately 80 %.

DISCUSSION

Structural welding simulations allow the prediction of geometrical deviations and accumulated residual stresses as well as their optimisation before conducting experiments. Due to the length of the multi-layer welds, calculation times for fully transient thermo-mechanical simulations are relatively long, the calculation stability suffers from a high number of bodies in contact elements in the model and the modelling effort is high, since the geometries need to be sliced and positioned layer-wise. Depending on the complexity of the models, the simulation times can vary from a few minutes to several days [15], [19]. The comparison of computational times used for the models is presented in Table 8. The simulations have been performed on an eight core 3.30 GHz i7-5820K processor with 32 GB installed RAM. All models have been calculated by using parallelisation, i.e., the calculation of one simulation is done in parallel using several CPU cores. Simufact supports two parallelisation options, namely domain decomposition method (DDM) and shared memory parallelisation (SMP) [20]. DDM subdivides the model into several sub-models that are connected with each other, whereas SMP allows one solver to use multiple cores.

Table 8 Computational time comparison between different models

Model	Adaptive mesh refinement	Parallelisation	Elements [-]	Computational time [h]
Single wall	no	yes	21,820	~ 24
Aerospace bracket	no	yes	61,612	~ 100

When comparing the single wall model and the aerospace bracket model in Table 8, it becomes obvious that, with increasing size and complexity of the models, the computational times increase gradually. Besides the model size, adaptive mesh refinement increases the computational costs by adding elements to the model. However, there are various ways to reduce computational times including adaptive mesh refinement and un-refinement, the use of symmetry in the models, parallel computing, reduced number of contact bodies and reasonable mesh sizes [15], [19], [21]. Efforts of software tool developers to implement dedicated direct energy deposition (DED) modules in the field of additive manufacturing help to fully exploit the potential of DED and make the calculation of complex models on an industrial scale economical [22].

CONCLUSION

Plasma metal deposition of large-scale Ti-6Al-4V multi-layer structures is investigated experimentally and numerically. A finite element simulation using Simufact Welding 8.0 is set-up to predict the mechanical behaviour of multi-layer components. Experiments are carried out in order to provide data for verifying the calculated temperature profiles and the out-of-plane distortion. Moreover, an airplane bracket is analysed to identify the optimal building strategy and to verify the simulation process for the industrial purpose. According to the results of this study, the following conclusions are drawn:

1. Based on experimental results, the Goldak double ellipsoid heat source model is verified to suit the experimental determined conditions. As an important feature for the application of structural welding simulations, more accurate temperature measurements for the heat source calibration are necessary. Improved temperature measurements can be addressed by using shielded thermocouples, different attachment techniques, higher frequency of data logging and the recording of the weld pool shape.
2. In the simulations, the thermal and mechanical boundary conditions are assumed to be constant throughout the deposition process. In fact, these parameters are not only temperature-dependent but also a function of the build height and geometry.
3. The results obtained from Simufact Welding 8.0 reproduce the distortion and temperature distribution of the experiment well. Discrepancies between simulation and experiment can occur due to inaccuracies in the calibration of the heat source, thermal and mechanical boundary conditions. Also, the level of detail in the modelling of the bead and wall geometry should be considered as influencing quantity. The weld bead profile for the deposition of the wall is modelled as a rectangle.

4. The virtual process development of the aerospace bracket emphasizes the potential of numerical simulations as digital twin to reduce the number of costly experimental trials.

APPENDICES

The following appendices are intended to roughly present how the mechanical boundary conditions for the thermo-mechanical simulation in Simufact Welding are determined.

MECHANICAL BOUNDARY CONDITIONS

Clamp stiffness

A linear elastic analysis using Abaqus CAE 6.14 is performed to estimate the spring stiffness of the clamp. The clamp consists of two parts, a steel step block and a steel step clamp. The clamp is loaded with an arbitrary constant force of 2,500 N acting on the negative of the surface that actually presses on the baseplate of the experimental setup described in "Materials and setup". The model is constrained by fixing all degrees of freedom of the bottom surface of the step block. The step block (master) and step clamp (slave) are connected using a surface-to-surface tie constraint. Isotropic material behaviour has been specified. A drawing of the model can be seen in Fig. 21 (a). The calculated deflection is set in relation with the force applied (Fig. 21 (b)). The slope of the linear curve yields the translational spring stiffness of the clamp.

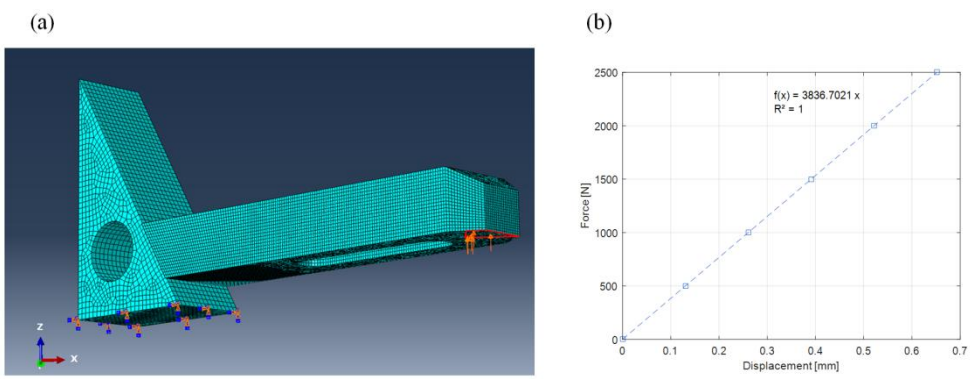

Fig. 21 (a) Meshed CAD model of the clamp assembly; (b) Force-Displacement relation of the clamp

To impose a mechanical boundary condition, the real clamping system is simplified, whereby the clamp is replaced by a spring with a corresponding spring stiffness. The spring stiffness is set to a constant value of 3,837 N/mm.

Contact force

To estimate the contact pressure of the clamp on the baseplate, another analysis using Abaqus CAE 6.14 is performed. The model consists of six parts, an aluminum backing plate, a titanium baseplate, a steel stud, a steel hexagonal flange nut, a steel step block and a steel step clamp. As outlined in "Materials and setup", the baseplates are fixed to the backing plate of the welding chamber by using clamps placed at specified positions. The steel bolts are pre-tensioned with a torque of 80 Nm. In Abaqus, the pretension is adjusted over the length, which is determined as the following: firstly, the flange nut is tightened manually until it makes contact with the clamp and, secondly, a torque wrench is used to apply a torque of 80 Nm, whereas the number of turns of the nut is counted. After about 5/8 turns, the required torque is reached. The thread pitch, which is 1.75 mm in the case of a M12 metric thread, multiplied by the number of turns is used as a satisfactory approximation to calculate the preload length of the screw. The stud is hence pre-tensioned with a length of 1.09 mm. The model is constrained by fixing all degrees of freedom of the bottom surface of the backing plate and symmetry boundary conditions on the cut surfaces. A drawing of the model can be seen in Fig. 22.

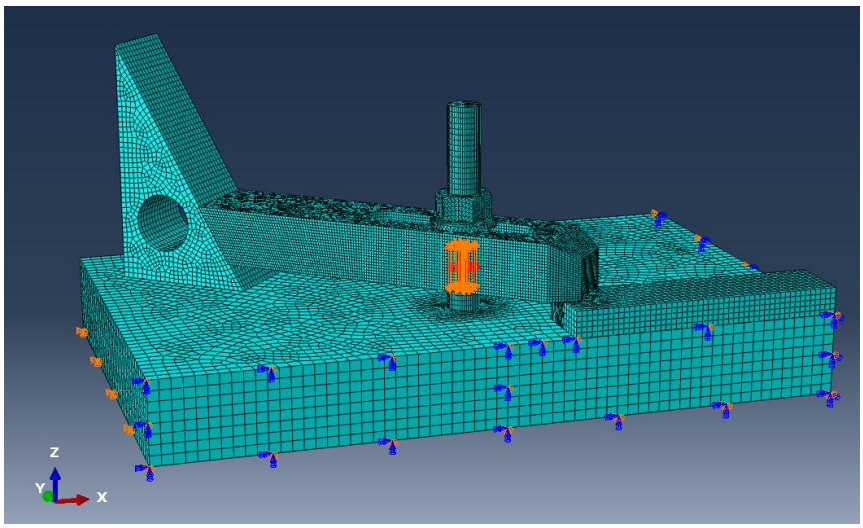

Fig. 22 Meshed CAD model of the contact force assembly

To reduce computational costs and time, firstly, isotropic material behaviour is assumed, and secondly, friction is only considered in the contact area of the clamp with the baseplate. All other interactions are modelled using a tie constraint. After the finite element model is solved, the average contact pressure at the baseplate of the surface in contact with the step clamp is determined. The average contact pressure is multiplied by the area of the surface to get the initial force applied on the baseplate. Since no static coefficient of friction for dry conditions is found for the material pairing steel-titanium, the contact behaviour is defined in a first step as frictionless. Then a value of 0.20 is

applied, which is a typical value for steel/steel dry contact [23]. At last, the friction coefficient is set to 0.36, which corresponds to a Ti-6Al-4V/Ti-6Al-4V contact pair [24].

Table 9 Contact force estimation

Friction-coefficient [-]	Mean contact pressure [MPa]	Contact surface area [mm²]	Mean contact force [kN]
frictionless	435.7	159.5	69.5
$\mu = 0.20$	424.0	159.5	67.6
$\mu = 0.36$	413.6	159.5	66.0

Table 9 shows the difference between frictionless and frictional contact. Since the baseplates have been machined prior to the PMD process and, therefore, have a good surface quality, the friction coefficient of 0.20 is used to calculate the contact force. Ultimately, the clamping movement can be controlled by "Stiffness & Force" with a constant stiffness of 3,837 N/mm and a constant contact force of 67,6 kN.

References

[1] T. WOHLERS, R. I. CAMPBELL, O. DIEGEL, J. KOWEN, N. MOSTOW and I. FIDAN: *Wohlers report 2022: 3D printing and additive manufacturing: global state of the industry*, Fort Collins, Colo: Wohlers Associates, 2022.

[2] F. MARTINA, J. MEHNEN, S. W. WILLIAMS, P. COLEGROVE and F. WANG: 'Investigation of the benefits of plasma deposition for the additive layer manufacture of Ti–6Al–4V', *J. Mater. Process. Technol.*, vol. 212, no. 6, pp. 1377-1386, Jun. 2012, doi: 10.1016/j.jmatprotec.2012.02.002.

[3] MARTIN BIELIK ET AL.: 'Plasma Metal Deposition in aerospace applications - Enabling a cost-efficient technology for high tech industries', Vienna, Austria, 2020.

[4] J. DING ET AL.: 'Thermo-mechanical analysis of Wire and Arc Additive Layer Manufacturing process on large multi-layer parts', *Comput. Mater. Sci.*, Jul. 2011, doi: 10.1016/j.commatsci.2011.06.023.

[5] P. A. COLEGROVE ET AL.: 'Microstructure and residual stress improvement in wire and arc additively manufactured parts through high-pressure rolling', *J. Mater. Process. Technol.*, vol. 213, no. 10, pp. 1782-1791, Oct. 2013, doi: 10.1016/j.jmatprotec.2013.04.012.

[6] N. HOYE, H. J. LI, D. CUIURI and A. M. PARADOWSKA: 'Measurement of Residual Stresses in Titanium Aerospace Components Formed via Additive Manufacturing', *Mater. Sci. Forum*, vol. 777, pp. 124-129, Feb. 2014, doi: 10.4028/www.scientific.net/MSF.777.124.

[7] F. MARTINA ET AL.: 'Residual stress of as-deposited and rolled wire+arc additive manufacturing Ti–6Al–4V components', *Mater. Sci. Technol.*, vol. 32, no. 14, pp. 1439-1448, Sep. 2016, doi: 10.1080/02670836.2016.1142704.

[8] H. E. COULES: 'Contemporary approaches to reducing weld induced residual stress', *Mater. Sci. Technol.*, vol. 29, no. 1, pp. 4-18, Jan. 2013, doi: 10.1179/1743284712Y.0000000106.

[9] J. GOLDAK, A. CHAKRAVARTI and M. BIBBY: 'A new finite element model for welding heat sources', *Metall. Trans. B*, vol. 15, no. 2, pp. 299-305, Jun. 1984, doi: 10.1007/BF02667333.

[10] 'Simufact Welding 2021', https://www.simufact.com/what-s-new-in-SW-v2021.html (accessed Jul. 17, 2022).

[11] 'Simufact Infosheet Heat Source'.

[12] M. MEGAHED, H.-W. MINDT, N. N'DRI, H. DUAN and O. DESMAISON: 'Metal additive-manufacturing process and residual stress modeling', *Integrating Mater. Manuf. Innov.*, vol. 5, no. 1, pp. 61-93, Dec. 2016, doi: 10.1186/s40192-016-0047-2.

[13] M. CHIUMENTI, M. CERVERA, A. SALMI, C. AGELET DE SARACIBAR, N. DIALAMI and K. MATSUI: 'Finite element modeling of multi-pass welding and shaped metal deposition processes', *Comput. Methods Appl. Mech. Eng.*, vol. 199, no. 37-40, pp. 2343-2359, Aug. 2010, doi: 10.1016/j.cma.2010.02.018.
[14] P. MICHALERIS: 'Modeling metal deposition in heat transfer analyses of additive manufacturing processes', *Finite Elem. Anal. Des.*, vol. 86, pp. 51-60, Sep. 2014, doi: 10.1016/j.finel.2014.04.003.
[15] R. MARTUKANITZ ET AL.: 'Toward an integrated computational system for describing the additive manufacturing process for metallic materials', *Addit. Manuf.*, vol. 1-4, pp. 52-63, Oct. 2014, doi: 10.1016/j.addma.2014.09.002.
[16] B. WU, Z. PAN, D. DING, D. CUIURI and H. LI: 'Effects of heat accumulation on microstructure and mechanical properties of Ti6Al4V alloy deposited by wire arc additive manufacturing', *Addit. Manuf.*, vol. 23, pp. 151-160, Oct. 2018, doi: 10.1016/j.addma.2018.08.004.
[17] N. HOYE, H. J. LI, D. CUIURI and A. M. PARADOWSKA: 'Measurement of Residual Stresses in Titanium Aerospace Components Formed via Additive Manufacturing', *Mater. Sci. Forum*, vol. 777, pp. 124-129, Feb. 2014, doi: 10.4028/www.scientific.net/MSF.777.124.
[18] 'Analytical Model for Distortion Prediction in Wire + Arc Additive Manufacturing', Oct. 2018, pp. 277-282. doi: 10.21741/9781945291890-44.
[19] J. DING ET AL.: 'Thermo-mechanical analysis of Wire and Arc Additive Layer Manufacturing process on large multi-layer parts', *Comput. Mater. Sci.*, Jul. 2011, doi: 10.1016/j.commatsci.2011.06.023.
[20] 'Simufact Infosheet Prallelsization'.
[21] P. HELBIG: 'Kalibrierung von Ersatzwärmequellen für die numerische Simulation von Laserschweißprozessen', Universität Kassel, 2018.
[22] Simufact Engineering Gmbh, 'Simufact Welding', *Simufact Welding*, Jan. 08, 2020, https://www.simufact.com/simufactwelding-welding-simulation.html (accessed Jan. 08, 2020).
[23] A. SCHWEIZER: 'Schweizer-FN', *Formelsammlung und Berechnungsprogramme Anlagenbau*, May 01, 2020, https://www.schweizer-fn.de/stoff/reibwerte/reibwerte.php (accessed Jan. 05, 2020).
[24] 'Coefficient of friction', May 01, 2020, http://www-eng.lbl.gov/~ajdemell/coefficients_of_friction.html (accessed Jan. 05, 2020).